Turbomachinery transient dynamics of radial rotor-stator contact occurrences with friction

Coline Jacobs, Mathias Legrand, Fabrice Thouverez, Patricio Almeida

Proceedings of ASME Turbo Expo 2023
Turbomachinery Technical Conference and Exposition

June, 26–30, 2023, Boston, Massachusetts

GT2023-102198

TURBOMACHINERY TRANSIENT DYNAMICS OF RADIAL ROTOR-STATOR CONTACT OCCURRENCES WITH FRICTION

Coline Jacobs[1,2,3], Mathias Legrand[1], Fabrice Thouverez[2], Patricio Almeida[3]

[1]McGill University,Structural Dynamics and Vibration Laboratory, Montreal, Canada
[2]Ecole Centrale Lyon, Laboratoire de Tribologie et Dynamique des Systèmes, Ecully, France
[3]Safran Helicopter Engines, Bordes, France

ABSTRACT

The present paper focuses on the numerical investigation of the transient response of a rotorshaft affected by unilateral contact occurrences with friction mechanisms. Rotor-stator contact is initiated radially at the shaft level. The components are modeled under the rigid bodies assumption and the rotor dynamical response is investigated in the time domain. The turbomachine is assumed to be driven by two torques: the first one is prescribed while the second one is induced by friction using Coulomb's model. Particular attention is paid to the accurate prediction of the unknown rotational speed transient. The proposed methodologies are grounded on the Carpenter and Moreau-Jean time-marching algorithms, implying the use of Lagrange multipliers to solve the frictional and unilateral contact conditions. The simplest procedure considers only sliding friction while the most sophisticated one involves convex analysis in order to deal with normal and friction forces independently is case of stiction. The solutions predicted by the algorithms are compared and show good agreement. The sensitivity study on the stator properties and friction coefficient allows the identification of the conditions affecting the rotational speed limitation. Based on the response post-processing in the time and frequency domains, it is found that a higher friction coefficient, a stiffer stator support or a lighter stator leads to a decrease of the rotational speed maximum value.

Keywords: time-marching, unilateral contact, rotor, stator, turbomachinery, rigid bodies, Coulomb's friction, rotational speed, transient dynamics

1. INTRODUCTION

Gas turbine engines are commonly used to power aircraft such as airplanes and helicopters. They can exhibit various designs yet always with four main areas involving the airflow: the compression side, the combustion chamber, the expansion side, and the secondary air system (SAS). The latter is a complex network of cavities where the gas turbine disks are immersed. After the combustion, burnt gases flowing through the turbine blading provide mechanical power to the shaft of which a part is used to drive the compressor. In the present work, only the turbine stage is considered. The turbine rotation axis is shifted radially with regard to the engine centerline which leads to the emergence of various contact zones. The first rotor-stator contact interface to appear, and of most interest, is located in the SAS. Contact occurs in a gasket mounted on the shaft upstream of the turbine bladed disc. Its nominal functions are to control the cooling airflow and to maintain an air pressure equilibrium along the shaft. The tightness is guaranteed by a ring although there still exist a gap about several hundreds of microns between the ring and its envelope. For the sake of simplicity, the sealing ring and the envelope are respectively called rotor and stator in the rest of the document. Subsequent blade-carter contacts occurrences are not accounted for. The main objective of this paper is to investigate the dynamical response of the shaft when rubbing in the seal occurs. The rotational velocity is an unknown of the problem affected by unilateral contact and frictional occurrences. In addition to the driving torque from aerodynamics, the turbomachine is subjected to a braking torque generated through frictional contact mechanisms.

The paper is organized as follows. Section 2 provides a literature overview on unilateral and frictional contact in rotordynamics. The turbine modeling and the derivation of the governing equations are presented in Section 3. In Section 4, the solution methods are detailed as well as the prerequisites for the gap assessment and the contributions of the unilateral and frictional contact efforts in the equations of motion. These methods are compared in Section 5 and applied to perform a parametric study on the friction coefficient, the stator support stiffness and the stator mass.

2. RUBBING IN TURBOMACHINES

Rotordynamics in presence of radial unilateral contact and friction is a research field widely investigated in literature [1–3]. The literature shows that a rotor confined within a stator might

generate rubbing mechanisms along with various and complex dynamical responses. Its center of gravity may orbit in the same direction as or opposite direction to the rotation of the engine. These two responses are called respectively forward and backward precessional motions [4]. Backward motion can be split into two subcategories that are: (1) *dry whirl* when the rotor rolls without slipping; (2) *dry whip* if the rotor rolls and slips. The latter is known to be "one of the more serious and destructive of the malfunctions that occur in rotating machinery" [5]. It should be noted that, in practice, the precessional motions can switch from forward to backward in an abrupt manner and it is possible that the rotor bounces on the neighboring components [4, 6]. Several parameters, such as friction coefficient and rotation speed [7, 8], affect the precessional response.

Also, gyroscopic terms, commonly ignored for simplicity, might have drastic consequences on the overall dynamics by coupling even further the nonlinear mechanisms in the response [9]. Another common assumption is to consider the rotation speed as constant or at least as a known function of time [4]. Instead, when frictional contact occurrences are involved, the torque is specified, at least on some interval of time, and the rotational velocity $\Omega(t)$ becomes an unknown of the problem [1, 2], as assumed in the present paper. This affects the governing equations, most notably the gyroscopic and stiffness matrices. They depend respectively on $\Omega(t)$ and its first derivative in time, along with the inertial forces inducing centrifugal stiffening effects [9].

2.1 Contact theory and friction

Unilateral contact conditions prevent mechanical bodies to penetrate each other and always creates a reaction force in the normal direction to the contact. A classical formulation relies on the Signorini conditions [10] expressed at the displacement level, stating that there exist two positive definite quantities, the normal force F_N and the normal distance d_N between the rotor and the stator, whose product equals zero at all times:

$$d_\mathrm{N} \geq 0, \quad F_\mathrm{N} \geq 0, \quad d_\mathrm{N} \cdot F_\mathrm{N} = 0. \tag{1}$$

The first inequality in Equation (1) reflects that penetration is not allowed while the second one means that traction between the bodies is prohibited. The above conditions can be condensed in a complementarity formulation

$$0 \leq d_\mathrm{N} \perp F_\mathrm{N} \geq 0. \tag{2}$$

In case of rubbing, there exists also a friction force valued with F_f which can be assessed by micro- or macro-models. Micro-models account for the surface condition. They may introduce time-dependency with kind of *friction memory* and hysteresis phenomena [11]. However, these models imply more parameters to identify and to calibrate by experiments [12]. Macro-models are preferred in the present study. They define the friction force opposed to the relative speed $\mathbf{v}_t$ between the bodies in contact. Its magnitude is commonly dictated by Coulomb's friction model involving the static and dynamic friction coefficients, μ_s and μ_d respectively, with the conditions

$$\begin{cases} |F_\mathrm{f}| = \mu_\mathrm{d} F_\mathrm{N} & \text{if } ||\mathbf{v}_t|| \neq 0 \\ |F_\mathrm{f}| \leq \mu_\mathrm{s} F_\mathrm{N} & \text{otherwise.} \end{cases} \tag{3}$$

In a vast majority of research works [3, 11, 13], and in the present paper as well, Coulomb's model is simplified by defining a single friction coefficient $\mu = \mu_\mathrm{s} \approx \mu_\mathrm{d}$.

2.2 Solution algorithms

Unilateral and frictional contact introduces a strong nonlinearity in the governing equations and dedicated numerical tool able to generate a meaningful approximate solution should be implemented. Transient phenomena being of prior interest in the present work, preference is given to time-domain integrators [14]. The combination of an integrator and the numerical treatment of the Signorini and Coulomb conditions led to the implementation of well-known algorithms such as the Moreau [15] or Carpenter [16] procedures. If the strict enforcement of Signorini conditions is desired, a regularization of the contact, like the penalty method [10], might not be appropriate. Instead, the use of Lagrange multipliers is possible, as achieved for instance in [1, 17] through Carpenter's algorithm. The Lagrange multiplier is a mathematical quantity that does not have necessarily any physical meaning. In Carpenter's algorithm, described further in the present document, the multiplier is associated to the normal contact force F_N. In Moreau-Jean procedure, the multiplier has the physical meaning of an impulse r_N.

The impenetrability condition is not the only one that should be satisfied in order to accurately model unilateral contact. At the instant of impact between two bodies, it is known that the normal velocity should satisfy an impact law guaranteeing the solution uniqueness. The most widely-used is the Newton impact law stating $v_\mathrm{N}^+ = -e v_\mathrm{N}^-$, where v_N^- (resp. v_N^+) represents the normal velocity right before (after) an impact, $e \in [0, 1]$ being a restitution factor. If $e = 0$, the impact is dissipative while $e = 1$ corresponds to an "elastic" impact and there is no energy loss [18]. Moreau [15] differentiated the Signorini conditions in time and the normal contact effort/distance relation from Equation (2) becomes an impulse r_N/normal velocity condition. The introduction of the Newton impact law in Equation (2) forms an expression of the unilateral contact constraints at velocity level, which reads

$$\begin{cases} 0 \leq (v_\mathrm{N}^+ + e v_\mathrm{N}^-) \perp r_\mathrm{N} \geq 0 & \text{if } d_\mathrm{N} < 0 \\ r_\mathrm{N} = 0 & \text{otherwise.} \end{cases} \tag{4}$$

This approach has the drawback to present residual penetration, issue solved in [19]. Also, the assessment of the friction force is another challenging task because of the nonsmoothness of the Coulomb model [18]. Works in rotordynamics, in a vast majority, consider that the relative tangential velocity on the contact interface never vanishes due to the high rotational speeds involved, and thus only *slipping* is accounted for [1, 7, 13, 17]. When sticking cannot be ignored, two dominant strategies to manage the multi-valued features of the law exist. The first approach is to regularize the Coulomb model: with a ramp function when the slip velocity goes under a user-defined tolerance [7] or with a tanh function [20]. The second approach uses mathematical concepts from convex analysis [21] and is further developed in the present document.

3. ROTOR-STATOR MODEL

3.1 System of interest

The rotor is composed of the turbine and rotor disks mounted on a shaft, see Figure 1. For a helicopter gas turbine, dimension the sealing ring (i.e. the rotor) radius is of several centimeters. The turbine, considered disconnected from the compressor and

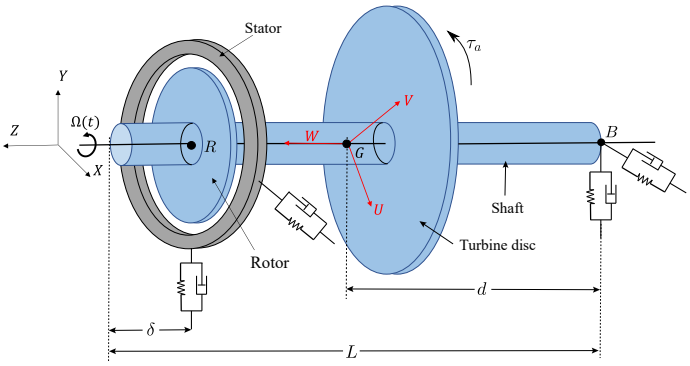

FIGURE 1: System of interest and reference frames

is only supported by the rear bearing, and by the stator through contact with the rotor disc (i.e. the sealing ring). The stator is an annular ring with linear and symmetric support located with distance δ from the shaft free extremity. In this paper, the shaft, the discs and the stator are all simplified as perfectly rigid. The bearings are defined by symmetric constant stiffness and damping. While the rigid bodies assumption is a first step to predict the rotordynamics with a few degrees of freedom, the uncoupling of the compressor and turbine stages is a configuration to be investigated on the real system as well. Aerodynamics aspects are out-of-scope in this research. Therefore, the driving torque applied to the turbine disc τ_a is set to a constant and the turbine's recoil due to the axial pressure gradient is neglected.

3.2 Mathematical model

3.2.1 Frames and coordinates systems. A rigid body commonly features six degrees-of-freedom (dofs): three translations for its center of mass G and three rotations. The frames involved in the definition of these rotations are detailed in Figures 1 and 2:

- (U, V, W): moving reference frame rigidly connected to the body, where W is the symmetry axis while U, V define the diametral axes.
- (X, Y, Z): fixed reference frame. The shaft center line initially coincides with the Z-axis.
- (x_1, y_1, z_1) and (x_2, y_2, z_2) are intermediate frames.

Hsieh & *al.* [22] defined the mobile frame with a first rotation by an angle ϕ about the Z-axis, followed by a second rotation by an angle α about $x_1 = x_2$, and finally a third one by an angle ψ about the W-axis. These rotations are illustrated in Figure 2. The authors also defined the angular displacements θ_x and θ_y by projection of the angle α, being small, on the $(X, Y)-$plane, *ie*

$$\theta_x = \alpha \cos\phi \quad \text{and} \quad \theta_y = \alpha \sin\phi. \tag{5}$$

The other consequence of the small angle assumption is that the resultant rotation about the W-axis is $\theta_w = \phi + \psi$. The rotational velocity $\Omega(t)$, of primary interest in the present work, corresponds to $\dot{\theta}_w$.

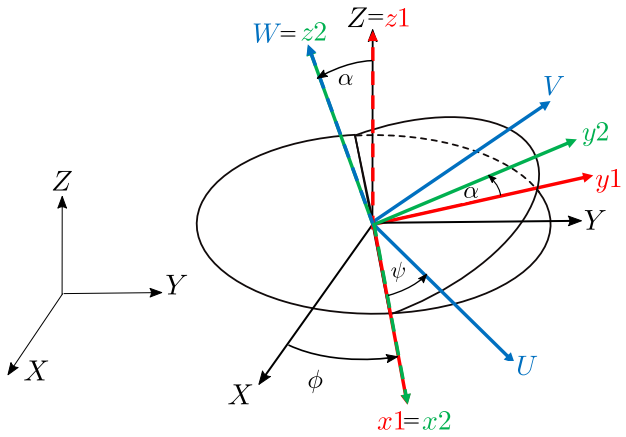

FIGURE 2: Rotations from fixed to moving reference frame [22]

3.2.2 Equations of motion. From Huygens' principle, the kinetic energy of a body of mass m with axial symmetry reads

$$2E_c = m(\dot{x}_G^2 + \dot{y}_G^2 + \dot{z}_G^2) + J_d(\omega_u^2 + \omega_v^2) + J_p\omega_w^2. \tag{6}$$

where J_d and J_p stand for diametral and polar mass moments of inertia. (x_G, y_G, z_G) correspond to the center of mass translations. As already said, no effort along the Z-direction is considered and the displacement z_G is removed from Equation (6). The quantities ω_u, ω_v and ω_w represent the rotational velocities components in the moving frame and are given by

$$\begin{cases} \omega_u = \dot{\alpha}\cos\psi + \dot{\phi}\sin\alpha\sin\psi \\ \omega_v = -\dot{\alpha}\sin\psi + \dot{\phi}\sin\alpha\cos\psi \\ \omega_w = \dot{\psi} + \dot{\phi}\cos\alpha. \end{cases} \tag{7}$$

By inserting Equations (5) and (7) into Equation (6), the kinetic energy becomes

$$2E_c = m(\dot{x}_G^2+\dot{y}_G^2)+J_d(\dot{\theta}_x^2+\dot{\theta}_y^2)+J_p\dot{\theta}_w^2+J_p\dot{\theta}_w(\dot{\theta}_x\theta_y-\dot{\theta}_y\theta_x). \tag{8}$$

For the contact treatment, the displacements at the rotor level (x_r, y_r) rather than center of mass are more appropriate. If the rotor has length L, points G and R are respectively located at a distance d and $L-\delta$ from the bearing B, and the translations q_G of point G are simplified to the linear interpolation

$$q_G = \nu q_r + (1-\nu)q_b \tag{9}$$

where $\nu = d/(L-\delta)$. The two angles θ_x and θ_y may also be expressed as functions of points R and B considering the first-order approximations

$$\theta_x \approx -\frac{y_r - y_b}{L-\delta} \quad \text{and} \quad \theta_y \approx \frac{x_r - x_b}{L-\delta}. \tag{10}$$

Consequently, the displacement of the rotor is defined by generalized coordinates $\mathbf{q}_T = (x_b, y_b, x_r, y_r, \theta)^\top$ where subscript w in the spinning rotation is dropped for simplicity. The kinetic energy becomes

$$\begin{aligned} 2E_c &= M_{11}(\dot{x}_b^2 + \dot{y}_b^2) + M_{22}(\dot{x}_r^2 + \dot{y}_r^2) + 2M_{12}(\dot{x}_b\dot{x}_r + \dot{y}_b\dot{y}_r) \\ &+ J_p\dot{\theta}^2 + H\dot{\theta}((\dot{y}_b - \dot{y}_r)(x_r - x_b) - (\dot{x}_r - \dot{x}_b)(y_b - y_r)) \end{aligned} \tag{11}$$

with $M_{11} = (1-\nu)^2 m + J_d/(L-\delta)^2$, $M_{12} = \nu(1-\nu)m - J_d/(L-\delta)^2$, $M_{22} = \nu^2 m + J_d/(L-\delta)^2$ and $H = J_p/(L-\delta)^2$. Gravity and bearing stiffness k_b contribute to the potential energy of the system in the following manner:

$$E_p = \frac{k_b}{2}(x_b^2 + y_b^2) + mg(\nu y_r + (1-\nu)y_b). \tag{12}$$

Without contact, the Lagrange equations yield the Ordinary Differential Equations (ODE)

$$\mathbf{M}_\mathrm{T}(\mathbf{q}_\mathrm{T})\ddot{\mathbf{q}}_\mathrm{T} + (\dot{\theta}\mathbf{G}_\mathrm{T} + \mathbf{D}_\mathrm{b})\dot{\mathbf{q}}_\mathrm{T} + \mathbf{K}_\mathrm{b}\mathbf{q}_\mathrm{T} = \mathbf{f}^\mathrm{ext}. \tag{13}$$

The terms $\mathbf{K}_\mathrm{b}$ and $\mathbf{D}_\mathrm{b}$ relate to the bearing stiffness and damping matrices while the mass matrix $\mathbf{M}_\mathrm{T}(\mathbf{q}_\mathrm{T})$, the gyroscopic matrix $\mathbf{G}_\mathrm{T}$ and external forces vector $\mathbf{f}^\mathrm{ext}$ are given by

$$\mathbf{M}(\mathbf{q}_\mathrm{T}) = \begin{pmatrix} M_{11} & 0 & M_{12} & 0 & H_y(\mathbf{q}_\mathrm{T}) \\ 0 & M_{11} & 0 & M_{12} & H_x(\mathbf{q}_\mathrm{T}) \\ M_{12} & 0 & M_{22} & 0 & -H_y(\mathbf{q}_\mathrm{T}) \\ 0 & M_{12} & 0 & M_{22} & -H_x(\mathbf{q}_\mathrm{T}) \\ H_y(\mathbf{q}_\mathrm{T}) & H_x(\mathbf{q}_\mathrm{T}) & -H_y(\mathbf{q}_\mathrm{T}) & -H_x(\mathbf{q}_\mathrm{T}) & J_p \end{pmatrix},$$

$$\mathbf{G}_\mathrm{T} = \begin{pmatrix} 0 & H & 0 & -H & 0 \\ -H & 0 & H & 0 & 0 \\ 0 & -H & 0 & H & 0 \\ H & 0 & -H & 0 & 0 \\ 0 & 0 & 0 & 0 & 0 \end{pmatrix}, \quad \mathbf{f}^\mathrm{ext} = \begin{pmatrix} 0 \\ -(1-\nu)mg \\ 0 \\ -\nu mg \\ \tau_\mathrm{a} \end{pmatrix} \tag{14}$$

with $H_x(\mathbf{q}_\mathrm{T}) = \frac{H}{2}(x_r - x_b)$ and $H_y(\mathbf{q}_\mathrm{T}) = -\frac{H}{2}(y_r - y_b)$. The stator is rigid and has two dofs: $\mathbf{q}_\mathrm{s} = (x_\mathrm{s}, y_\mathrm{s})^\top$. Its dynamics is governed by the classical linear ODE

$$\mathbf{M}_\mathrm{s}\ddot{\mathbf{q}}_\mathrm{s} + \mathbf{D}_\mathrm{s}\dot{\mathbf{q}}_\mathrm{s} + \mathbf{K}_\mathrm{s}\mathbf{q}_\mathrm{s} = \mathbf{0}. \tag{15}$$

with

$$\mathbf{M}_\mathrm{s} = \begin{pmatrix} m_\mathrm{s} & 0 \\ 0 & m_\mathrm{s} \end{pmatrix}, \quad \mathbf{D}_\mathrm{s} = \begin{pmatrix} c_\mathrm{s} & 0 \\ 0 & c_\mathrm{s} \end{pmatrix}, \quad \mathbf{K}_\mathrm{s} = \begin{pmatrix} k_\mathrm{s} & 0 \\ 0 & k_\mathrm{s} \end{pmatrix}.$$

By grouping Equations (13) and (15), the whole system is defined by mass, gyroscopic, damping and stiffness matrices (resp. $\mathbf{M}, \mathbf{G}, \mathbf{D}, \mathbf{K}$) of size 7×7 with the combination of the above generalized coordinates $\mathbf{q} = (\mathbf{q}_\mathrm{T}, \mathbf{q}_\mathrm{s})^\top$, which gives

$$\mathbf{M}(\mathbf{q})\ddot{\mathbf{q}} + (\dot{\theta}\mathbf{G} + \mathbf{D})\dot{\mathbf{q}} + \mathbf{K}\mathbf{q} = \mathbf{f}^\mathrm{ext}. \tag{16}$$

4. NUMERICAL SOLUTION METHODS

4.1 Gap and contact efforts directions

A preliminary task to any contact solution method is the assessment of the distance between the bodies. A front view of the rigid rotor of radius R_r confined within the stator (of radius R_s) is proposed in Figure 3. The point s corresponds to the stator center. For rigid bodies, the minimal distance is obtained along the **sr** vector between point p and its projection p' along the normal unit vector **n** on the stator. The normal distance d_N is defined by a scleronomous relation

$$d_\mathrm{N} = R_s - R_r - ||\mathbf{sr}|| = g_0 - \sqrt{(x_r - x_s)^2 + (y_r - y_s)^2} \tag{17}$$

between the generalized coordinates $\mathbf{q} = (x_b, y_b, x_r, y_r, \theta, x_s, y_s)$ and with g_0 being the initial gap value equal to $R_s - R_r$.

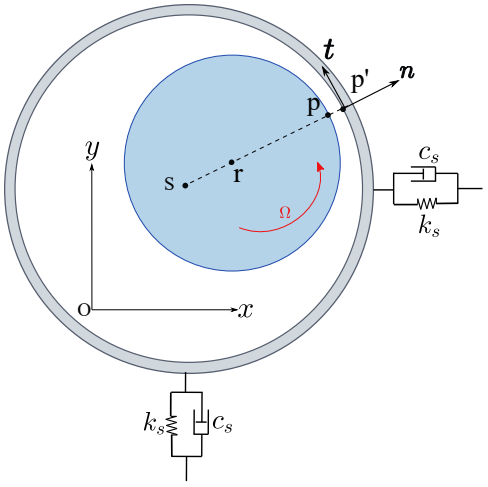

FIGURE 3: Gap and contact local frame

The analytic expression of the normal distance allows the identification of the vector $\mathbf{C}_\mathrm{N}$, which reflects the contribution of the Lagrange multiplier F_N to the equations of motion. Since the effort F_N is acting along the normal direction, $\mathbf{C}_\mathrm{N}$ is equal to the normal distance gradient $\nabla_\mathbf{q} d_\mathrm{N}$ and yields

$$\mathbf{C}_\mathrm{N} = \left(0, 0, \frac{x_s - x_r}{||\mathbf{sr}||}, \frac{y_s - y_r}{||\mathbf{sr}||}, 0, \frac{x_r - x_s}{||\mathbf{sr}||}, \frac{y_r - y_s}{||\mathbf{sr}||}\right)^\top. \tag{18}$$

When friction is considered, it is oriented along the tangential unit vector **t** in Figure 3 which must be defined as well. The friction force contribution to the equations of motion is provided by the vector $\mathbf{C}_\mathrm{T}$, orthogonal to $\mathbf{C}_\mathrm{N}$, which gives

$$\mathbf{C}_\mathrm{T} = \left(0, 0, \frac{y_r - y_s}{||\mathbf{sr}||}, \frac{x_s - x_r}{||\mathbf{sr}||}, -R_r, \frac{y_s - y_r}{||\mathbf{sr}||}, \frac{x_r - x_s}{||\mathbf{sr}||}\right)^\top. \tag{19}$$

Note that the component $-R_r$ reflects the braking torque induced by friction. Consequently, the contact efforts acting within the system (rotor and stator) and denoted $\mathbf{f}^c \in \mathbb{R}^7$, are computed as

$$\mathbf{f}^c = \mathbf{C}_\mathrm{N} \cdot F_\mathrm{N} + \mathbf{C}_\mathrm{T} \cdot F_\mathrm{f} \tag{20}$$

The contact efforts vector is added to Equation (16) to form the governing ODE with contact occurrence

$$\mathbf{M}(\mathbf{q})\ddot{\mathbf{q}} + (\dot{\theta}\mathbf{G} + \mathbf{D})\dot{\mathbf{q}} + \mathbf{K}\mathbf{q} = \mathbf{f}^\mathrm{ext} + \mathbf{f}^c. \tag{21}$$

It can be noted that the above procedure can be extended to the case of multiple contact points. As a result, each point k is assigned to a pair of Lagrange multipliers. There are k gap functions, $(F_\mathrm{N}, F_\mathrm{f})$ are both replaced by vectors of size k, and $\mathbf{C}_\mathrm{N}$ and $\mathbf{C}_\mathrm{T}$ are defined as rectangular matrices with k columns.

4.2 Carpenter Algorithm

This method is selected for its simplicity of implementation while satisfying the non-penetration constraint. The main steps of the Carpenter algorithm are the following: the time-domain $t = [t_s, t_e]$ is discretized by t_i, $i = 0, \ldots, N$ spaced with time step $h = (t_e - t_s)/N$. From this discretization, we define the unknowns

$\mathbf{q}_i \approx \mathbf{q}(t_i)$. The time derivatives are approximated via the explicit centered finite difference scheme

$$\dot{\mathbf{q}}_i = \frac{\mathbf{q}_{i+1} - \mathbf{q}_{i-1}}{2h} \quad \text{and} \quad \ddot{\mathbf{q}}_i = \frac{\mathbf{q}_{i+1} - 2\mathbf{q}_i + \mathbf{q}_{i-1}}{h^2}. \tag{22}$$

This integrator requires initial conditions for the two first time steps, $\mathbf{q}_0$ and $\mathbf{q}_1$. Equation (22) is inserted in Equation (21) which provides the expression $\bar{\mathbf{M}}(\theta_{i+1})\mathbf{q}_{i+1} - \bar{\mathbf{D}}\mathbf{q}_i + \bar{\mathbf{K}}(\theta_{i+1})\mathbf{q}_{i-1} = \mathbf{f}_i^{\text{ext}} + \mathbf{f}_i^{c}$ with

$$\begin{aligned} \bar{\mathbf{M}}(\theta_{i+1}) &= \frac{\mathbf{M}(\mathbf{q_i})}{h^2} + \frac{\left(\frac{\theta_{i+1} - \theta_{i-1}}{2h}\right)\mathbf{G} + \mathbf{D}}{2h} \\ \bar{\mathbf{D}} &= \frac{2\mathbf{M}(\mathbf{q_i})}{h^2} - \mathbf{K} \\ \bar{\mathbf{K}}(\theta_{i+1}) &= \frac{\mathbf{M}(\mathbf{q_i})}{h^2} - \frac{\left(\frac{\theta_{i+1} - \theta_{i-1}}{2h}\right)\mathbf{G} + \mathbf{D}}{2h}. \end{aligned} \tag{23}$$

In the present work, the mass matrix $\mathbf{M}$ is function of the known turbine displacements $\mathbf{q}_i$ (see Equations (13) and (21)) and $\mathbf{M}(\mathbf{q}_i)$ must be updated at each time step. Note that matrices $\bar{\mathbf{M}}$ and $\bar{\mathbf{K}}$ are functions of θ_{i+1}, because of the time discretization of the unknown rotational velocity $\dot{\theta}_i$ in Equation (22). As already said, rotation θ is part of the generalized coordinates vector $\mathbf{q}$ but dependencies of matrices to this degree-of-freedom are made explicit[1]. Then, three tasks are completed for each time step $n = 1, \ldots, N-1$:

- Prediction of the contact-free displacement vector by solving

$$\mathbf{q}_{i+1}^{\text{p}} = \bar{\mathbf{M}}(\theta_{i+1}^{\text{p}})^{-1}\left[\bar{\mathbf{D}}\mathbf{q}_i - \bar{\mathbf{K}}(\theta_{i+1}^{\text{p}})\mathbf{q}_{i-1} + \mathbf{f}_i^{\text{ext}}\right]. \tag{24}$$

- Gap computation d_{N}^{p} through Equation (17) and penetration check ($d_{\text{N}}^{\text{p}} < 0$).
- Correction applied to $\mathbf{q}_{i+1}^{\text{p}}$ if a penetration is detected. For simplicity, we assume only one point of contact with the corresponding gap $d_{\text{N},i+1}^{\text{p}}$. In the present method, only one Lagrange multiplier $F_{\text{N},i+1}$ is involved. The Coulomb friction force in sliding phase is $F_{\text{f},i+1} = -\mu\,\text{sign}(\mathbf{v}_t \cdot \mathbf{t})F_{\text{N},i+1}$. The contributions of this sole multiplier to the dynamics is then given by the vector $\mathbf{C}_{\text{NT}}$ which is a combination of $\mathbf{C}_{\text{N}}$ and $\mathbf{C}_{\text{T}}$ such as

$$\mathbf{C}_{\text{NT}} = \mathbf{C}_{\text{N}} - \mu\,\text{sign}(\mathbf{v}_t \cdot \mathbf{t})\mathbf{C}_{\text{T}}. \tag{25}$$

  Correction is achieved simultaneously in the normal and tangential directions through the equations

$$\begin{cases} F_{\text{N},i+1} = -(\mathbf{C}_{\text{N}}^{\top}\bar{\mathbf{M}}(\theta_{i+1})^{-1}\mathbf{C}_{\text{NT}})^{-1} d_{\text{N},i+1}^{\text{p}}, \\ \mathbf{q}_{i+1} = \mathbf{q}_{i+1}^{\text{p}} + \bar{\mathbf{M}}(\theta_{i+1})^{-1}\mathbf{C}_{\text{NT}}F_{\text{N},i+1}. \end{cases} \tag{26}$$

Due to the unknown rotational velocity $\dot{\theta}_i$ (and θ_{i+1}) in Equation (23), Equations (24) and (26) are coupled and nonlinear in $\mathbf{q}_{i+1}$ and a dedicated nonlinear solver must be introduced. In this paper, two versions of Carpenter's algorithm were implemented in Python.

- The first one, named `Carp-QN`, was introduced in [1]. The entire Carpenter algorithm, Equations (17), (24) and (26), is embedded within a quasi-Newton loop and is fully iterative. All three prediction, verification and correction steps are applied at most `itMax` times.
- The second one, called `Carp-oneVC` and introduced in this work, is a simplification of the above method considering that the time step h is small. Equation (24) for prediction is solved by calling the Python function `fsolve`[2]. It finds the root of a nonlinear function through a Newton loop given an initial guess $\mathbf{q}_{i+1}^{0}$. In other words, the prediction step remains iterative. For each time step, the first guess is computed through Equation (23), without contact and assuming that angular acceleration is linear. Therefore two initial angular accelerations γ_0 and γ_1 should be defined. Given the predicted solution $\mathbf{q}_{i+1}^{\text{p}}$, the rotor-stator distance $d_{\text{N},i+1}^{\text{p}}$ is assessed and the solution is corrected if needed. The procedure detailed in Algorithm 1 completes a verification and a correction step at most once. This approach is faster but introduces an error since the matrix $\bar{\mathbf{M}}(\theta_{i+1}^{\text{p}})$ is computed with the predicted rotation angle only.

Algorithm 1 `Carp-oneVC`

Require: $i \leftarrow 0$, $\mathbf{q}_0$ and $\ddot{\theta}_0 \leftarrow \gamma_0$
Require: $i \leftarrow 1$, $\mathbf{q}_1$ and $\ddot{\theta}_1 \leftarrow \gamma_1$
for $i = 1, \ldots, N-1$ **do**
  {Assumption of linear angular acceleration}
  $\ddot{\theta}_{i+1}^{0} \leftarrow 2\ddot{\theta}_i - \ddot{\theta}_{i-1}$
  {Contactless initial guess}
  $\theta_{i+1}^{0} \leftarrow \ddot{\theta}_{i+1}^{0} h^2 + 2\theta_i - \theta_{i-1}$
  $\mathbf{q}_{i+1}^{0} \leftarrow \bar{\mathbf{M}}(\theta_{i+1}^{0})^{-1}\left[\bar{\mathbf{D}}\mathbf{q}_i - \bar{\mathbf{K}}(\theta_{i+1}^{0})\mathbf{q}_{i-1} + \mathbf{f}_i^{\text{ext}}\right]$
  {Nonlinear solver: finds solution $\mathbf{q}_{i+1}^{\text{p}}$ of Equation (24) with initial guess $\mathbf{q}_{i+1}^{0}$}
  Solve $\bar{\mathbf{M}}(\theta_{i+1}^{\text{p}})\mathbf{q}_{i+1}^{\text{p}} - \left[\bar{\mathbf{D}}\mathbf{q}_i - \bar{\mathbf{K}}(\theta_{i+1}^{\text{p}})\mathbf{q}_{i-1} + \mathbf{f}_i^{\text{ext}}\right] = \mathbf{0}$
  {Gap computation through Equation (17)}
  $d_{\text{N},i+1}^{\text{p}} \leftarrow g_0 - \sqrt{(x_{r,i+1}^{\text{p}} - x_{s,i+1}^{\text{p}})^2 + (y_{r,i+1}^{\text{p}} - y_{s,i+1}^{\text{p}})^2}$
  if $d_{\text{N},i+1}^{\text{p}} \geq 0$ **then**
    {No correction}
    $F_{\text{N},i+1} \leftarrow 0$
    $F_{\text{f},i+1} \leftarrow 0$
    $\mathbf{q}_{i+1} \leftarrow \mathbf{q}_{i+1}^{\text{p}}$
  else
    {Correction}
    $F_{\text{N},i+1} \leftarrow -(\mathbf{C}_{\text{N}}^{\top}\bar{\mathbf{M}}(\theta_{i+1}^{\text{p}})^{-1}\mathbf{C}_{\text{NT}})^{-1} d_{\text{N},i+1}^{\text{p}}$
    $F_{\text{f},i+1} \leftarrow -\mu\,\text{sign}(\mathbf{v}_t \cdot \mathbf{t})F_{\text{N},i+1}$
    $\mathbf{q}_{i+1} \leftarrow \mathbf{q}_{i+1}^{\text{p}} + \bar{\mathbf{M}}(\theta_{i+1}^{\text{p}})^{-1}\mathbf{C}_{\text{NT}}F_{\text{N},i+1}$
  end if
  {Update (θ_{i+1} is in $\mathbf{q}_{i+1}$)}
  $\ddot{\theta}_{i+1} \leftarrow (\theta_{i+1} - 2\theta_i + \theta_{i-1})/h^2$
end for

[1] Since θ_{i+1} belongs to vector $\mathbf{q}_{i+1}$, writing the matrices $\bar{\mathbf{M}}(\mathbf{q}_{i+1})$ and $\bar{\mathbf{K}}(\mathbf{q}_{i+1})$ would also be appropriate.

[2] https://docs.scipy.org/doc/scipy/reference/generated/scipy.optimize.fsolve.html

4.3 Moreau-Jean algorithm and Siconos

The Moreau-Jean algorithm can be used in order to propose a reference solution method that involves all sources of nonsmoothness: the Signorini conditions at speed level and the Coulomb friction model with sticking phase considered.

First of all, in order to admit a nonsmooth solution, equations of motions (16) must be differentiated in time between two neighbor instants spaced by $\mathrm{d}t$, as performed in [3]. By denoting $\mathbf{C}(\mathbf{v}) = \dot{\theta}\mathbf{G} + \mathbf{D}$, the governing equations become

$$\begin{cases} \mathbf{M}(\mathbf{q})d\mathbf{v} + [\mathbf{C}(\mathbf{v})\mathbf{v} + \mathbf{K}\mathbf{q} - \mathbf{f}^{\mathrm{ext}}]\mathrm{d}t = \mathrm{d}\mathbf{f}^{\mathrm{c}} \\ \dot{\mathbf{q}} = \mathbf{v} \end{cases} \tag{27}$$

where $\mathrm{d}\mathbf{v}$ and $\mathrm{d}\mathbf{f}^{\mathrm{c}}$ define speed and contact effort variations. Equation (27) is then discretized with an integrator from the θ-method family (with parameter denoted γ to not be confused with rotation θ). However, integrating non-linear terms imply more developments detailed in section 10.1.2 of [18]. The smooth terms $[\mathbf{C}(\mathbf{v})\mathbf{v} + \mathbf{K}\mathbf{q} - \mathbf{f}^{\mathrm{ext}}]$ are collected in the vector $\mathbf{f}(\mathbf{q}, \mathbf{v}, t)$. With $\mathrm{d}t$ set to the time step h, the governing equations become

$$\begin{cases} \mathbf{M}(\mathbf{q}_{i+\eta})(\mathbf{v}_{i+1} - \mathbf{v}_i) + h\widetilde{\mathbf{f}}_{i+\gamma} = \mathbf{r}_{i+1}, \\ \mathbf{q}_{i+1} = \mathbf{q}_i + h((1-\gamma)\mathbf{v}_i + \gamma\mathbf{v}_{i+1}) \end{cases} \tag{28}$$

with

$$\begin{cases} \widetilde{\mathbf{f}}_{i+\gamma} = (1-\gamma)\mathbf{f}(\mathbf{q}_i, \mathbf{v}_i, t_i) + \gamma\mathbf{f}(\mathbf{q}_{i+1}, \mathbf{v}_{i+1}, t_{i+1}), \\ \mathbf{q}_{i+\eta} = (1-\eta)\mathbf{q}_i + \eta\mathbf{q}_{i+1}. \end{cases} \tag{29}$$

Note that the impulse quantity $\mathbf{r}_{i+1}$ is related to contact efforts by the integral $\int \mathrm{d}\mathbf{f}^{\mathrm{c}}$. In this case, the Lagrange multiplier has the physical meaning of a normal impulse r_{N} instead of the normal force F_{N}, as already said in Section 2. Similarly, a frictional impulse r_{f} is defined.

The last line of Equation (29) reflects that the non-linear mass matrix is evaluated with a weighted interpolation of the displacement vector $\mathbf{q}$ where the weight parameter is denoted η. Then, the dynamics is linearized and the solution $\mathbf{v}_{i+1}$ is computed through an Newton loop with the iteration matrix $\widetilde{\mathbf{M}} = \mathbf{M}(\mathbf{q}_{i+\eta}) + h\gamma\nabla_{\mathbf{v}}\mathbf{f}(\mathbf{q}, \mathbf{v}, t) + h^2\gamma^2\nabla_{\mathbf{q}}\mathbf{f}(\mathbf{q}, \mathbf{v}, t)$. The last two terms are the Jacobian matrices of the smooth terms with respect to displacement $\mathbf{q}$ and $\mathbf{v}$. If the ODE was linear time invariant, one would retrieve the classical iteration matrix $\widetilde{\mathbf{M}} = \mathbf{M} + h\gamma\mathbf{D} + h^2\gamma^2\mathbf{K}$ used for instance in [3].

The prediction step is the same as in Carpenter's algorithm, except that the predicted quantity is the velocity $\mathbf{v}^{\mathrm{p}}_{i+1}$ and not directly the displacement. For the correction step, the normal effort F_{N} and the friction force F_{f} (and so, the related impulses) may be independent in case of *dry whirl* (i.e. sticking friction) and thus two distinct Lagrange multipliers must be introduced. They are grouped into the vector $\mathbf{\Lambda}_{i+1} = (r_{\mathrm{N}}, r_{\mathrm{f}})^{\top}_{i+1}$ whose domain of definition is a cone of slope μ, also known as *Coulomb's cone* K, illustrated in Figure 4 for a 2D contact. As a result, the contact efforts in the fixed frame are $\mathbf{r}_{i+1} = (\mathbf{C}_{\mathrm{N}}\mathbf{C}_{\mathrm{T}})\mathbf{\Lambda}_{i+1}$ and the expression of the corrected speed is

$$\mathbf{v}_{i+1} = \mathbf{v}^{\mathrm{p}}_{i+1} + \widetilde{\mathbf{M}}^{-1}\left(\mathbf{C}_{\mathrm{N}}\mathbf{C}_{\mathrm{T}}\right)\mathbf{\Lambda}_{i+1}. \tag{30}$$

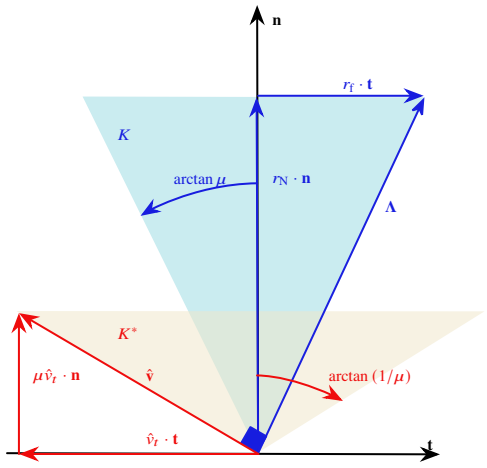

FIGURE 4: Coulomb cone and SOCCP for slipping [18]

In order to incorporate the Newton impact law, the term $e_{\mathrm{N}}\mathbf{v}_i$ is added to both sides of Equation (30) and the result is projected on the normal direction in the contact reference frame. This projected speed is defined in discrete time by $\hat{v}_{\mathrm{N},i+1} := \mathbf{C}^{\top}_{\mathrm{N}}(\mathbf{v}_{i+1} + e_{\mathrm{N}}\mathbf{v}_i)$ and depends on $\mathbf{\Lambda}$ with

$$\hat{v}_{\mathrm{N},i+1} = \mathbf{C}^{\top}_{\mathrm{N}}\widetilde{\mathbf{M}}^{-1}(\mathbf{C}_{\mathrm{N}}, \mathbf{C}_{\mathrm{T}})\mathbf{\Lambda}_{i+1} + \mathbf{C}^{\top}_{\mathrm{N}}(\mathbf{v}^{\mathrm{p}}_{i+1} + e_{\mathrm{N}}\mathbf{v}_i). \tag{31}$$

Since friction is accounted for, an impact law along the tangential direction must also be defined, involving another restitution coefficient e_{t} [18, 23]. The above procedure is repeated which leads to the definition of the projected tangential speed $\hat{v}_{t,i+1} := \mathbf{C}^{\top}_{\mathrm{T}}(\mathbf{v}_{i+1} + e_{\mathrm{t}}\mathbf{v}_i)$, also computed with

$$\hat{v}_{t,i+1} = \mathbf{C}^{\top}_{\mathrm{T}}\widetilde{\mathbf{M}}^{-1}(\mathbf{C}_{\mathrm{N}}, \mathbf{C}_{\mathrm{T}})\mathbf{\Lambda}_{i+1} + \mathbf{C}^{\top}_{\mathrm{T}}(\mathbf{v}^{\mathrm{p}}_{i+1} + e_{\mathrm{t}}\mathbf{v}_i). \tag{32}$$

Denoting the modified local speed by $\hat{\mathbf{v}} = (\hat{v}_{\mathrm{N}} + \mu|\hat{v}_t|, \hat{v}_t)^{\top}$ (index i is dropped for simplicity) and introducing the symbol $\perp$ that represents orthogonality between $\hat{\mathbf{v}}$ and contact efforts, the Signorini-Coulomb conditions imply to solve, at every time step, the complementarity problem

$$K^* \ni \hat{\mathbf{v}} \perp \mathbf{\Lambda} \in K \tag{33}$$

where K^* is the dual of cone K. The system formed by Equations (31) to (33) is known as a Second Order Cone Complementarity Problem (SOCCP) [18], which is illustrated for a sliding contact in Figure 4.

The procedure described above is available in `Siconos` [24]. `Siconos` is a C++ numerical tool dedicated to nonsmooth problems. In this program, a *projected* version of Moreau-Jean algorithm is available too [19]. The term *projected* means that the solution strictly satisfies both Signorini conditions at speed and displacement levels.

To summarize, four solution methods are selected in the present paper with features listed in Table 1. Concerning the restitution factor e_{N}, it is not explicitly defined in Carpenter algorithm. The method is equivalent to work with a fully dissipative impact. As a result, for sake of comparison, the impact law in Moreau-Jean algorithms (`Sic-Mor` and `Sic-Proj`) is $e_{\mathrm{N}} = e_{\mathrm{t}} = 0$.

Name	Friction	Signorini (contact law)	
		Displacement	Velocity
`Carp-oneVC`	Sliding	Yes	No
`Carp-QN`	Sliding	Yes	No
`Sic-Mor`	Total	No	Yes
`Sic-Proj`	Total	Yes	Yes

TABLE 1: Contact solvers and properties

5. RESULTS

A reference case is first defined and run for the four proposed solution algorithms. The friction coefficient is set to 0.1 and the time step, to $h = 10^{-6}$ s. Time is normalized by a reference time t_{ref}. The same solution is predicted by all four solvers, hence only the response for `Sic-Proj` is presented in Section 5. Partial contact takes place at the beginning since separations emerge, see Figure 5(b). After $0.80t_{\text{ref}}$, the normalized distance d_N/g_0 vanishes, meaning that contact becomes permanent. The relative

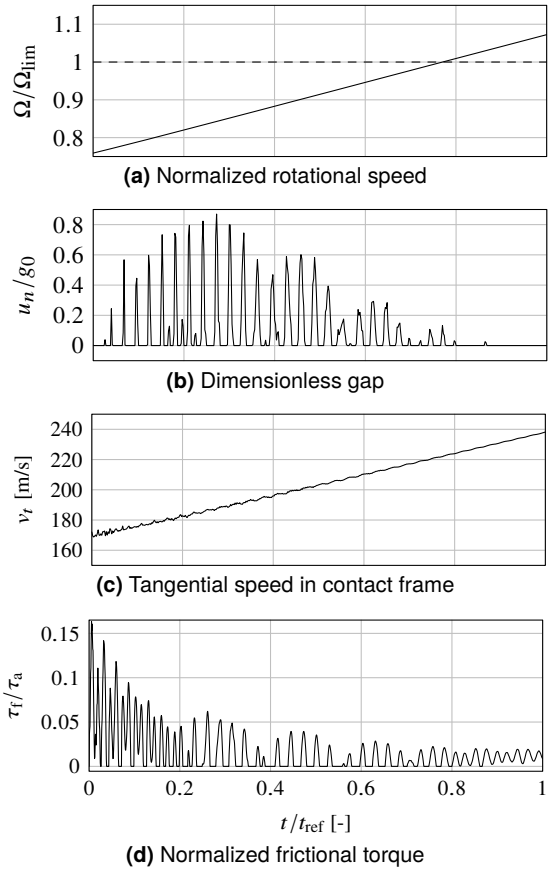

(a) Normalized rotational speed

(b) Dimensionless gap

(c) Tangential speed in contact frame

(d) Normalized frictional torque

FIGURE 5: Time response for reference case with `Sic-Proj`

velocity in tangential direction is never zero (see Figure 5(c)), reflecting *dry whip*, with $F_f = \mu F_N$. The friction torque is plotted in Figure 5(d) and normalized by the aerodynamic torque τ_a. It turns out that this ratio is always smaller than unity and the turbine rotational velocity thus increases. Figure 5(a) shows that the maximal authorized velocity Ω_{lim} is reached at $t = 0.76t_{\text{ref}}$.

In the remainder, two contact solvers are selected: `Sic-Proj` since it involves all the constraints management and `Carp-oneVC` for its smaller CPU compared to `Carp-QN` for identical results. The next sections focus on parameter studies in order to identify in which conditions overspeed is safely limited. The sensitivity of the dynamics to three quantities μ, k_s and m_s is investigated.

5.1 Sensitivity to friction coefficient

5.1.1 Time domain. Speed transients in Figure 6 show that the rotational velocity stays under Ω_{lim} for $\mu > 0.22$. Even if

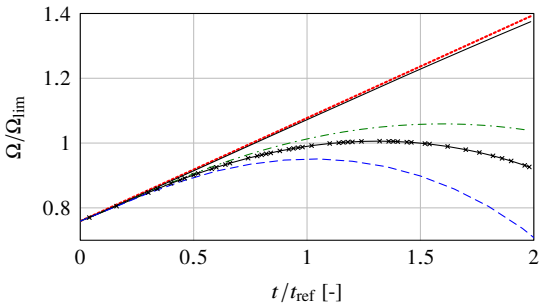

FIGURE 6: Sensitivity of rotational velocity to friction coefficient: $\mu = 0$ (----), $\mu = 0.1$ (ref) (——), $\mu = 0.2$ (- - -), $\mu = 0.22$ (—×—) , $\mu = 0.25$ (– – –)

the speed transients for the frictionless case and the reference case $\mu = 0.1$ are similar, these two simulations predict different dynamics. When analyzing precessional speeds (see Figure 7(a)) for the frictionless case, it turns out that v_{prec} converges to positive values, reflecting a forward precessional motion. However, the type of precesionnal motion becomes of less interest here since contact separation takes place for $t > 0.85t_{\text{ref}}$ (see Figure 7(c)). For $\mu = 0.1$, the precessional speed is subjected to an abrupt transition between forward (positive) and backward (negative) precessional motions. For $t > 1.3t_{\text{ref}}$, the precessional speed is still oscillating but remains always negative, reflecting transition to dry whip. However this transitions takes place too late to affect the rotational speed transient. For $\mu = 0.25$, see Figure 7(a), the precessional speed shows more negative value with regard to reference case. The mean value decreases with friction coefficient and v_{prec} becomes always negative for $t > 1.15t_{\text{ref}}$. In other words, the higher the friction coefficient, the more dominant the *backward* precessional motion. As already said, this phenomenon comes with larger unilateral contact efforts, which is confirmed by the increase of the frictional torque in Figure 7(b).

5.1.2 Frequency analysis. Rotordynamics can also be investigated through the spectral content of the solution. A spectrogram is a frequency analysis tool displaying the time evolution of a spectrum $X(f,t)$ (f being the frequency) related to signal $x(t)$ through Fourier transform. In the present document, the spectrograms of two time signals related to perpendicular displacements (for instance along X and Y axes) are combined to assess a *merged* spectrogram $XY(f,t)$. This particular time-frequency diagram is derived from *full*-spectrum [25] and is used in [12] to provide information about vibratory amplitudes and related frequency content, along with the direction of the precessional motion. A peak lying in the positive (resp. negative) frequency domain reflects occurrence of forward (resp. backward) precessional motion. In the present document, full-spectrograms are obtained by taking rotor displacements (x_r, y_r) for vibration signals in time domain.

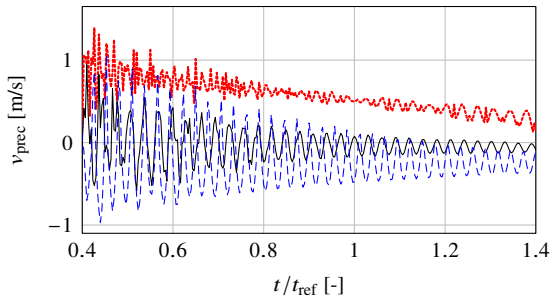

(a) Precessional speed

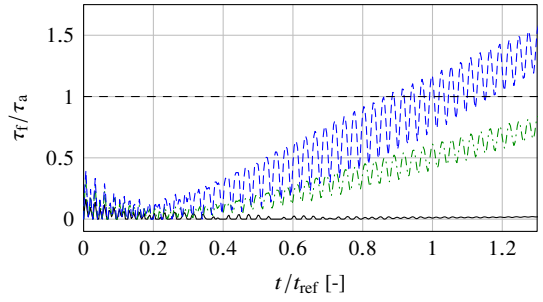

(b) Normalized frictional torque

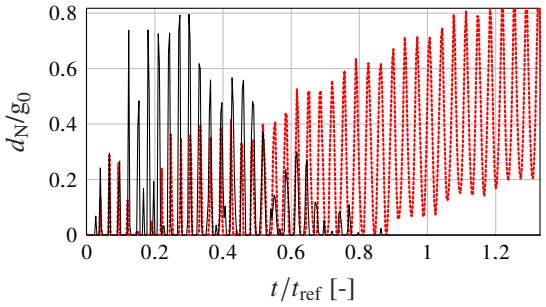

(c) Normalized gap

FIGURE 7: Response sensitivity to friction coefficient: $\mu = 0$ (----), $\mu = 0.1$ (ref) (——), $\mu = 0.2$ (– – –), $\mu = 0.25$ (– – –)

The eigenfrequencies of the coupled rotor-stator system should first be identified. In the present document, rotor and stator are considered coupled by setting stator displacements (x_s, y_s) equal to the rotor displacements (x_r, y_r). This approach is equivalent to add the stator mass at the rotor level. The eigenfrequencies are function of the rotational velocity through gyroscopic effects, see Equation (13). Therefore, the rotational velocity is imposed $\Omega = \dot{\theta}$ in a range going from 0 to Ω_{lim}. The resulting system has four dofs (x_b, y_b, x_r, y_r) and as many eigenfrequencies being functions of the rotational velocity. They are displayed in the Campbell diagram in Figure 8. For each rotational speed are calculated four positive eigenvalues. At rest, there exist two double modes of natural frequencies denoted f_1 and f_2, which then split into forward (subscript f) and backward (subscript b) modes. The Campbell diagram can be used to determine the eigenfrequencies with respect to time implicitly through $\Omega(t)$. At instant t, $\Omega(t)$ is assessed and reported in the Campbell diagram to evaluate the eigenfrequencies. The resulting curves are thus $f(\Omega(t))$. Negatives values $-f(\Omega(t))$ are considered as well for response investigation in negative frequencies domain in case of backward precessional motion. These curves are then superimposed to the

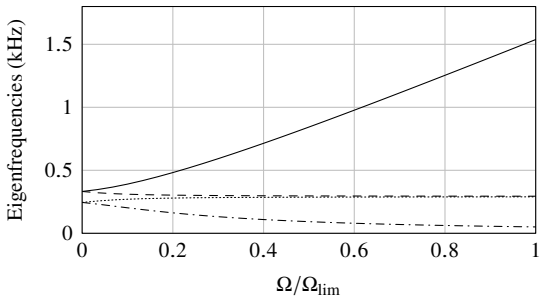

FIGURE 8: Campbell diagram: eigenfrequencies for coupled turbine and stator, f_{1b} (– – –), f_{1f}(----), f_{2b}(– –), f_{2f}(——)

merged spectrogram of the rotor vibration.

Figure 9(a) corresponds to the frictionless case and shows a superposition between the spectrogram and the second forward precession mode f_{2f}, reflecting a vibratory resonance of the forward precessional motion There are no other matches between the frequency content of rotor vibration and modes, although the other peaks remain close. The highest peak lies in the positive frequency domain at 190 Hz, confirming the occurrence of a forward precessional motion. Note that after $0.9t_{ref}$, the peaks of low magnitude vanish. Spectrograms are powerful tools able to reflect nonlinear and or transitions phenomena [12]. However, the type of the transition phenomenon at causing the spectrum modification cannot be identified by the sole investigation in frequency domain. In the present case, the steep variation of frequency content is due to contact separation after $0.9t_{ref}$ (see Figure 7(c)).

Spectrogram and time evolution of eigenfrequencies for the reference case $\mu = 0.1$ are displayed in Figure 9(b). At the beginning of the simulation ($t < 0.2t_{ref}$), there still exists a vibratory resonance on the second forward mode f_{2f} and the highest peak is located at 190 Hz. However, the spectrum in the low-frequency range tends to become symmetric with respect to the zero frequency, which confirms equipartition between forward and backward precessional motions in the rotor response. Towards the end of the simulation, the highest peak is found approximately at −15 Hz meaning that a backward precessional motion emerges, in agreement with Figure 7(a). Note that the lowest peaks suddenly vanish for time after $0.8t_{ref}$. This phenomenon was already visible for frictionless case but this time, the transition in frequency content corresponds to a permanently closed contact, as confirmed by Figure 7(c). The various spectrograms exhibit changes in the dynamics for both $\mu = 0$ and $\mu = 0.1$ but are not capable to discriminate between transition from partial contact to permanent contact (cf. $\mu = 0.1$) or to contact separation (cf. $\mu = 0$). To this end, the frequency-domain analysis should be complemented by investigations in directly in the time domain.

A longer simulation is thus run for $\mu = 0.25$ where the rotational velocity stays under the allowed limit. The corresponding spectrogram is shown in Figure 9(c). At the beginning of the simulation, there exists a superposition between the spectrum and the second forward mode f_{2f} only. For $t > 0.7t_{ref}$, two superpositions appear with the backward modes (f_{1b} and f_{2b}) in the negative frequency range. The associated peaks become dominant

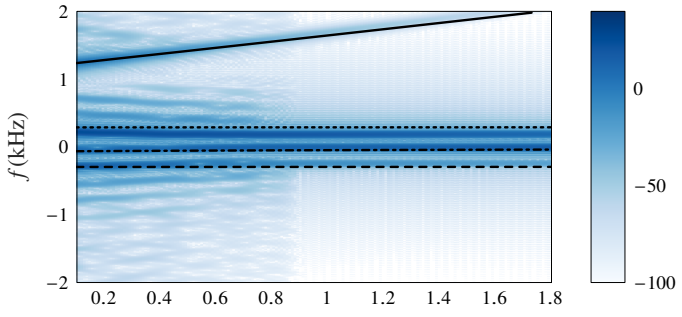

(a) $\mu = 0$

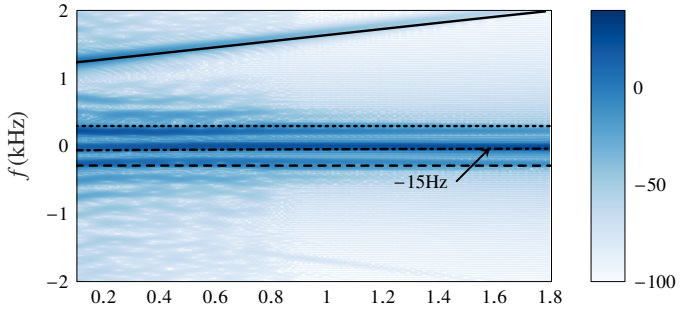

(b) $\mu = 0.1$ [reference]

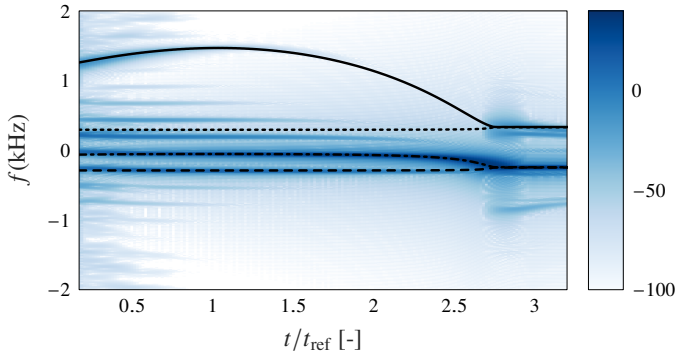

(c) $\mu = 0.25$

FIGURE 9: Rotor response spectrograms $XY(f,t)$ and time evolution of eigenfrequencies: f_{1b} (- - -), f_{1f} (- - - -), f_{2b} (– –), f_{2f} (——)

and confirms the resonance of the backward precessional motion. Around $2.7t_{ref}$, secondary peaks arise and reflect a transition from dry whip to dry whirl. Note that when the rotor is decelerating, which is the case here, the frequencies of forward and backward motions tend to the same value for each mode: $f_{1b}(t) \approx f_{1f}(t)$ and $f_{2b}(t) \approx f_{2f}(t)$ for $t > 2.6t_{ref}$. This effect is only caused by the decrease of $\Omega(t)$. Gyroscopic effects become less important and the forward and backward modes exhibit similar frequencies.

5.2 Sensitivity to the stator support stiffness

In this section, the friction coefficient is set back to 0.1 and the stator stiffness k_s is varied. The stiffnesses to be tested, denoted with the symbol $*$, are made non-dimensional through a division by the reference stiffness $k_{s,ref}$. Figure 10 shows that the normalized rotational velocity $\Omega/\Omega_{lim} \geq 1$ during the entire simulation only for $k_s^* > 5$.

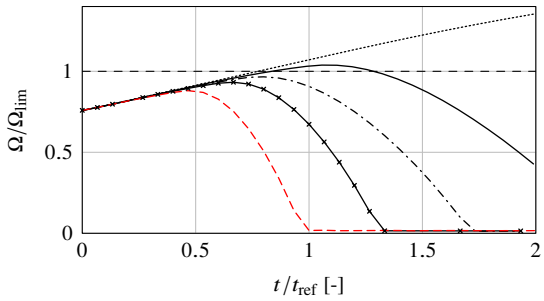

FIGURE 10: Rotational speed transients: $k_s^* = 4$ (- - - -), 5 (——), 6 (- - -), 8 (–✕–) and 10 (– –)

The friction torque is plotted in Figure 11(a) for $k_s^* = 10$. When $t < 0.45t_{ref}$, contact is partial since the torque vanishes for short periods of time. During closed contacts, the friction torque generated is smaller than the driving torque but steadily increases. For $t > 0.45t_{ref}$, the friction torque never vanishes and contact becomes permanent. Moreover, it overcomes the torque induced by the aerodynamical forces so that the rotational speed decreases. The increased friction torque can be explained by the precessional speed displayed in Figure 11(b). Indeed, for $t > 0.5t_{ref}$, precessional speed becomes strictly negative and keeps decreasing: dry whip is taking place. This is confirmed by the spectrogram in Figure 12. The main peak corresponds to a negative frequency (≈ -109 Hz) and superimposes with the first rear mode f_{1b}. Another main peak appears at ≈ -500 Hz which remains close to the second backward mode f_{2b} for $t > 0.75t_{ref}$. When contact is partial, the frequency content of the rotor vibration is richer but still shows good agreement with the eigenfrequencies of the coupled system. As already noticed in Figure 9(c), the spectrogram shows the emergence of additional secondary peaks when $t \geq t_{ref}$. This phenomenon is related to a transition from dry whip to pure rolling of the rotor. the presence of dry whirl is also confirmed in Figure 11(c) showing the relative tangential velocity at the contact location. One can observe a major difference between `Carp-oneVC`, only accounting for sliding, and `Sic-Proj`. With `Carp-oneVC`, the relative velocity remains small but switches between negative to positive values. Instead, `Sic-Proj` and the treatment of the true Coulomb model, strictly satisfies pure rolling motion conditions. However, the corresponding spectrograms are in good agreement.

5.3 Modification of stator mass

The present section investigates how the stator mass affects the dynamical response of the system. A parameter study is conducted on m_s, k_s and μ. The stator mass is normalized by a reference mass $m_{s,ref}$ and three values are tested: a reference $m_s^* = 1$ along with $m_s^* = 2.10$ and $m_s^* = 3.15$. The friction coefficient is set to the reference value $\mu = 0.1$. For each mass above, the stiffness k_s starts at k_{ref} and increased. A simulation is run with same duration and the maximum rotational speed Ω_{max} is found. Results for both `Carp-oneVC` and `Sic-Proj` are reported in Figure 13(a). It turns out that, for the considered masses, the increase of k_s leads to a decrease of Ω_{max}. For the reference mass $m_s^* = 1$, as already said, the maximum rotational velocity remains

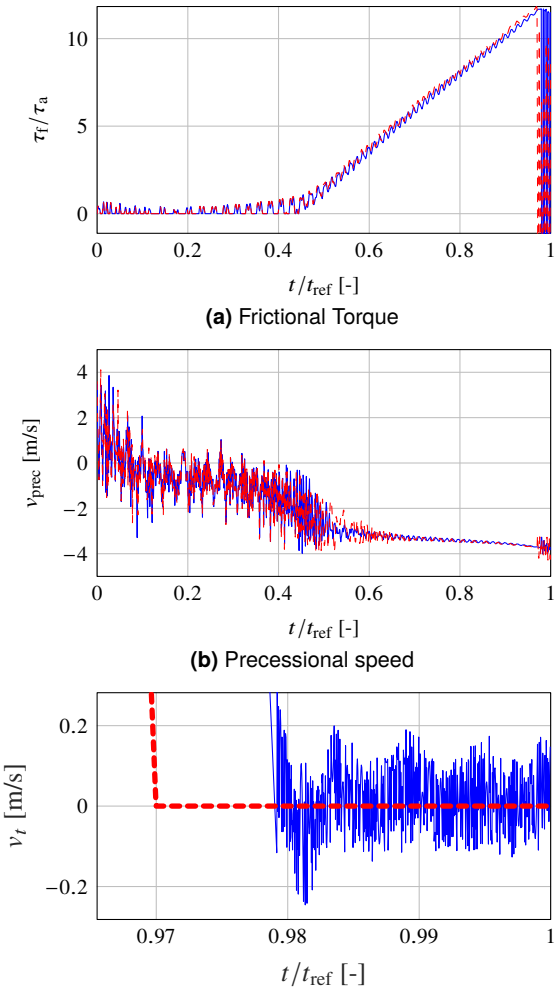

(a) Frictional Torque

(b) Precessional speed

(c) Relative tangential speed: focus on dry whirl

FIGURE 11: Time responses for $k_s^* = 10$: `Carp-oneVC` (——) and `Sic-Proj` (– –)

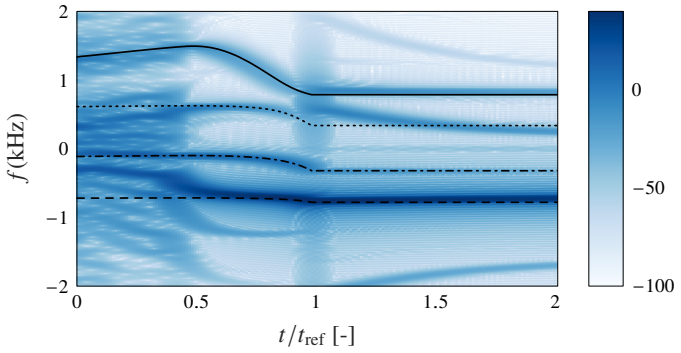

FIGURE 12: Spectrogram $XY(f,t)$ for $k_s = 10k_{s,ref}$ and time evolution of eigenfrequencies: $f_{1b}(\Omega(t))$ (– – –), $f_{1f}(\Omega(t))$(– · – ·), $f_{2b}(\Omega(t))$(– –), $f_{2f}(\Omega(t))$(——)

under Ω_{lim} as soon as $k_s > 5.5k_{s,ref}$. This effect reduces when the mass increases. Indeed, for $m_s^* = 2.10$, the maximum speed no longer monotonously decreases with k_s. However, there are still operating parameters for which rotational speed limitation is obtained. For the largest mass, the stiffness needs to be further

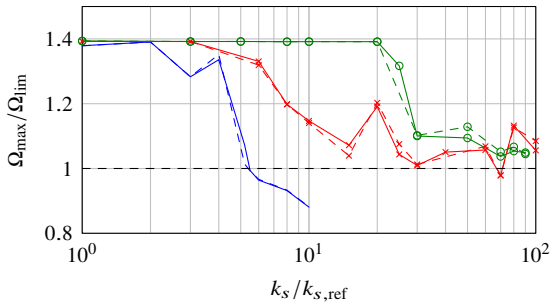

(a) $\mu = 0.1$: `Carp-oneVC` (dashed) and `Sic-Proj` (solid)

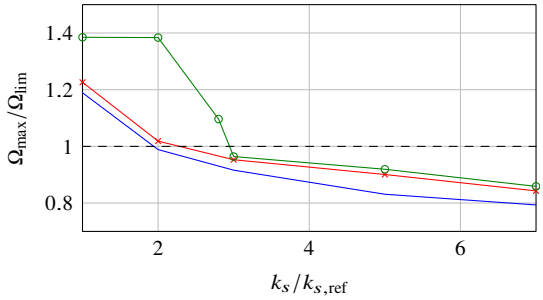

(b) $\mu = 0.17$: `Sic-Proj` only

FIGURE 13: Maximum rotational speed-stiffness diagram for three stator masses: $m_s^* = 1$ (——), $m_s^* = 2.10$ (–×–) and $m_s^* = 3.15$ (–o–)

increased to induce a decrease of Ω_{max}. However, it is not possible to find a realistic stiffness guaranteeing $\max(\Omega(t))/\Omega_{lim} < 1$. The same conclusions are drawn for both solvers which provide similar results with slight differences when the mass increases. These differences are expected since, if impacts do not occur exactly at the same instant, solvers provide distinct responses.

For $\mu = 0.17$, Figure 13(b) shows again that a stiffer stator leads to a reduced $\max(\Omega(t))$. Results are shown for the `Sic-Proj` solver only but equivalent solutions were predicted with `Carp-oneVC`. For all masses, there is a stiffness threshold for which $\max(\Omega(t)) \leq \Omega_{lim}$ is achieved. Accordingly, the combined increase of μ and k_s implies a rotor deceleration even for the highest mass. This threshold increases with mass and decreases with μ. For instance, for the reference mass, the limitation is satisfied for $k_s > 2k_{s,ref}$ instead of $5.5k_{s,ref}$.

To summarize, a large friction coefficient and a stiff stator support lead to a rotorshaft deceleration for the largest set of stator masses. However, the friction coefficient is the most difficult variable to control and identify.

6. CONCLUSION

Contact treatment with Lagrange multipliers in time domain is implemented to predict the transient response of the rigid rotor and stator. The unknown rotational velocity makes the resolution non trivial due to gyroscopic effects and algorithms must be adapted. The present paper confirms that approaches based on Carpenter and Moreau-Jean algorithms show results in agreement. Variations in the friction coefficient, the stator stiffness at supports and the stator mass govern the occurrence of backward precessional motion which is in agreement with literature [5]. The subsequent increase of the contact efforts, commonly to be

avoided have a strong influence on the rotational velocity. For a well-chosen set of parameters, the braking torque generated by friction overcomes the driving torque from aerodynamics. The rotational speed is then bounded and the rotor is able to slow down. Existence of a backward precessional motion is also confirmed through frequency analysis. A frequency-domain study also shows that spectral content of the dynamics coincides with coupled rotor-stator modes.

ACKNOWLEDGMENTS

The authors are grateful to Safran Helicopter Engines for providing the financial support for this project, and for giving permission to publish this work.

NOMENCLATURE

m	Mass [kg]
k	Stiffness [N/m]
c	Damping [N s/kg]
F	force [N]
r	Impulse [N s]
e	Restitution factor [-]
d	Local distance [m]
h	Time step [s]
f	Frequency [Hz]
τ	Torque [N m]
μ	Coulomb friction coefficient [-]
Ω	Angular velocity [rad/s]
g_0	Initial gap [m]
t_{ref}	Simulation reference time [s]
Ω_{lim}	Rotational velocity limit [rpm]
(X, Y, Z)	Fixed frame
(U, V, W)	Moving frame connected to center of mass
(J_d, J_p)	Diametral and polar mass moments of inertia
(x, y)	Displacements in X and Y directions
(ϕ, α, ψ)	Rotation angles from fixed to moving frame
$(\theta_x, \theta_y, \theta_w)$	Rotation angles about X, Y and W axes
$\mathbf{v}$	Generalized velocity coordinates [m/s]
$\mathbf{q}$	Generalized displacement coordinates [m,rad]
$\mathbf{v}_t$	Tangential relative speed at contact level[m/s]
$\mathbf{f}^{\text{ext}}$	Generalized external efforts vector [N,N m]
$\mathbf{f}^c$	Generalized contact efforts vector [N,N m]
$\mathbf{n}, \mathbf{t}$	Normal and tangential unit vectors in contact local frame

Superscripts and subscripts

i	discrete time index
N	normal component
t	tangential component
f	friction
T	turbine
G	center of mass
s	stator
r	rotor
b	bearing
ref	reference
p	predicted

REFERENCES

[1] Roques, S., Legrand, M., Cartraud, P., Stoisser, C. and Pierre, C. "Modeling of a rotor speed transient response with radial rubbing." *Journal of Sound and Vibration* Vol. 329 No. 5 (2010): pp. 527–546. DOI 10.1016/j.jsv.2009.09.016.

[2] Dai, X., Jin, Z. and Zhang, X. "Dynamic Behavior of the full rotorstop rubbing: numerical simulation and experimental verification." *Journal of Sound and Vibration* Vol. 251 No. 5 (2002): pp. 807–822. DOI 10.1006/jsvi.2001.3998.

[3] Thorin, A., Guérin, N., Legrand, M., Thouverez, F. and Almeida, P. "Nonsmooth Thermoelastic Simulations of Blade–Casing Contact Interactions." *Journal of Engineering for Gas Turbines and Power* Vol. 141 No. 2 (2018). DOI 10.1115/1.4040857.

[4] Lalanne, M. and Ferraris, G. *Rotordynamics prediction in engineering*, 2nd ed. John Wiley (1998).

[5] Muszyńska, A. *Rotordynamics*. Mechanical engineering ; 188, Taylor & Francis (2005).

[6] Jacquet-Richardet, G., Torkhani, M., Cartraud, P., Thouverez, F., Nouri Baranger, T., Herran, M., Gibert, C., Baguet, S., Almeida, P. and Peletan, L. "Rotor to stator contacts in turbomachines. Review and application." *Mechanical Systems and Signal Processing* Vol. 40 No. 2 (2013): pp. 401–420. DOI 10.1016/j.ymssp.2013.05.010.

[7] Chen, S.L. and Géradin, M. "Finite element simulation of nonlinear transient response due to rotor-stator contact." *Engineering Computations* Vol. 14 No. 6 (1997): pp. 591–603. DOI 10.1108/02644409710180356.

[8] Srivastava, A., Tiwari, M. and Singh, A. "Identification of rotor-stator rub and dependence of dry whip boundary on rotor parameters." *Mechanical Systems and Signal Processing* Vol. 159 (2021): p. 107845. DOI 10.1016/j.ymssp.2021.107845.

[9] Genta, G. *Dynamics of rotating systems*. Mechanical engineering series, Springer (2005).

[10] Wriggers, P. *Computational contact mechanics*, 2nd ed. Springer (2006).

[11] Pennestrì, E., Rossi, V., Salvini, P. and Valentini, P.P. "Review and comparison of dry friction force models." *Nonlinear Dynamics* Vol. 83 No. 4 (2016): pp. 1785–1801. DOI 10.1007/s11071-015-2485-3.

[12] Duran, C., Manin, L., Andrianoely, M.-A., Bordegaray, C., Battle, F. and Dufour, R. "Effect of Rotor-Stator Contact on the Mass Unbalance Response." Pennacchi, P. (ed.). *Proceedings of the 9th IFToMM International Conference on Rotor Dynamics*: pp. 1965–1975. 2015. Springer International Publishing. DOI 10.1007/978-3-319-06590-8_163.

[13] Legrand, M., Pierre, C., Cartraud, P. and Lombard, J.-P. "Two-dimensional modeling of an aircraft engine structural bladed disk-casing modal interaction." *Journal of Sound and Vibration* Vol. 319 No. 1-2 (2009): pp. 366–391. DOI 10.1016/j.jsv.2008.06.019.

[14] Géradin, M. and Rixen, D. *Mechanical vibrations : theory and application to structural dynamics*. Wiley (2014).

[15] Moreau, J.-J. "Unilateral contact and dry friction in finite freedom dynamics." J.-J., Moreau and P.D, Panagiotopoulos (eds.). *Nonsmooth Mechanics and Applications*. Vol. 302 of *International centre for mechanical sciences*. Springer (1988): pp. 1–82. DOI 10.1007/978-3-7091-2624-0_1.

[16] Carpenter, N.J., Taylor, R.L. and Katona, M.G. "Lagrange constraints for transient finite element surface contact." *International Journal for Numerical Methods in Engineering* Vol. 32 No. 1 (1991): pp. 103–128. DOI 10.1002/nme.1620320107.

[17] Almeida, P., Gibert, C., Thouverez, F. and Ousty, J.-P. "On some physical phenomena involved in blade-casing contact." *9th*

International Conference on Structural Dynamics (EURODYN 2014). 2014. URL https://hal.archives-ouvertes.fr/hal-02121521.

[18] Acary, V. and Brogliato, B. *Numerical methods for nonsmooth dynamical systems*. 35, Springer (2008).

[19] Acary, V. "Projected event-capturing time-stepping schemes for nonsmooth mechanical systems with unilateral contact and Coulomb's friction." *Computer Methods in Applied Mechanics and Engineering* Vol. 256 (2013): pp. 224–250. DOI 10.1016/j.cma.2012.12.012.

[20] Draganis, Andreas. "Finite Element Modeling of Transient Thermomechanical Rolling Contact Featuring Mixed Control of the Rigid Body Motion." *Journal of Tribology* Vol. 139 No. 1 (2017): p. 011503. DOI 10.1115/1.4033048.

[21] Acary, V., Brémond, M. and Huber, O. "On Solving Contact Problems with Coulomb Friction: Formulations and Numerical Comparisons." Leine, R., Acary, V. and Brüls, O. (eds.). *Advanced Topics in Nonsmooth Dynamics* (2018): pp. 375–457. DOI 10.1007/978-3-319-75972-2_10.

[22] Hsieh, S-C., Chen, J-H. and Lee, A-C. "A modified transfer matrix method for the coupling lateral and torsional vibrations of symmetric rotor-bearing systems." *Journal of Sound and Vibration* Vol. 289 No. 1-2 (2006): pp. 294–333. DOI 10.1016/j.jsv.2005.02.004.

[23] Zhang, S., Gui, N., Huang, X., Ge, L., Yang, X., Tu, J. and Jiang, S. "Verifying the tangential and normal restitution coefficients for double-sphere particles." *Powder Technology* Vol. 363 (2020): pp. 419–427. DOI 10.1016/j.powtec.2020.01.025.

[24] Acary, V., Bonnefon, O., Brémond, M., Huber, O., Pérignon, F. and al. "An introduction to Siconos." Technical Report No. RT-0340. INRIA. 2019. URL https://hal.inria.fr/inria-00162911v3.

[25] Muszyńska, A. and Goldman, P. "Application of full spectrum to rotating machinery diagnostics." *Orbit First Quarter* (1999): pp. 17–21.